AGU PUBLICATIONS

Global Biogeochemical Cycles

RESEARCH ARTICLE
10.1002/2016GB005476

Anthropogenic carbon in the ocean—Surface to interior connections

Sjoerd Groeskamp[1], Andrew Lenton[2,3], Richard Matear[2], Bernadette M. Sloyan[2], and Clothilde Langlais[2]

[1]Lamont-Doherty Earth Observatory, Columbia University, New York, New York, USA, [2]CSIRO Oceans and Atmospheres, Hobart, Tasmania, Australia, [3]Antarctic Climate and Ecosystems Cooperative Research Centre, University of Tasmania, Hobart, Tasmania, Australia

Key Points:
- New diagnostic revealing Anthropogenic Carbon circulation pathways
- Separated contribution from seasonality, advection, trend, surface fluxes, and mixing
- Anthropogenic carbon accumulation mainly at interface between SAMW and AAIW

Correspondence to:
S. Groeskamp,
sjoerdgroeskamp@gmail.com

Citation:
Groeskamp, S., A. A. Lenton, R. J. Matear, B. Sloyan, and C. Langlais (2016), Anthropogenic carbon in the ocean—Surface to interior connections, *Global Biogeochem. Cycles*, *30*, 1682–1698, doi:10.1002/2016GB005476.

Received 30 DEC 2015
Accepted 9 OCT 2016
Accepted article online 20 OCT 2016
Published online 10 NOV 2016

Abstract Quantifying the surface to interior transport of anthropogenic carbon (C_A) is critical for projecting future carbon uptake and for improved understanding of the role of the oceans in the global carbon cycle. Here we develop and apply a diagnostic tool that provides a volumetric stream function in (C_A, σ_0) coordinates to calculate the total diapycnal C_A transport in the ocean, where σ_0 is the surface referenced potential density anomaly. We combine this with air-sea fluxes of C_A to infer the internal ocean mixing of C_A to obtain a closed globally integrated budget analyses of the ocean's C_A transport. This diagnostic separates the contribution from the mean flow, seasonal cycles, trend, surface fluxes, and mixing in the distribution and the accumulation of C_A in the ocean. We find that the redistribution of C_A from the surface to the interior of the ocean is due to an interplay between circulation and mixing. The circulation component is dominated by the mean flow; however, effects due to seasonal cycles are significant for the C_A redistribution. The two most important pathways for C_A subduction are through the transformation of thermocline water (TW) into subantarctic mode water and by transformation of Circumpolar Deep Water (CDW) into lighter Antarctic Intermediate Water. The results suggest that an accurate representation of intermediate and mode water formation, deep water formation, and spatial and temporal distribution of ocean mixing in ocean models is essential to simulate and project the oceanic uptake of C_A.

1. Introduction

Atmospheric concentrations of carbon dioxide (CO_2) continue to rise at unprecedented rates as a result of human activities, with current anthropogenic carbon (C_A) emissions at nearly 10 Pg C_A yr^{-1} [*Ciais et al.*, 2013]. About 30% of total emissions since the pre-industrial period has been taken up and stored in the ocean [*Ciais et al.*, 2013]. By absorbing C_A from the atmosphere, the oceans play a key role in slowing the rate of climate change. Therefore, understanding how the oceans sequester C_A is crucial for our ability to predict the future climate.

C_A enters the ocean through air-sea gas exchange at a rate set by differences in partial pressures between the surface ocean and the atmosphere and proportional to the surface wind speed. Despite the important role of air-sea gas exchange, the rate limiting step in the oceanic uptake of C_A is the upper ocean to interior transport of C_A [*Matear*, 2001; *Iudicone et al.*, 2011]. The rate of C_A sequestration by the ocean is related to the large-scale dynamics, which controls the ventilation of the interior ocean. Using a numerical model, *Bopp et al.* [2015] suggest 90% of the absorbed C_A is subducted through the base of the mixed layer, and both advection and diapycnal mixing play an important role.

Observational studies of C_A have traditionally focussed on detecting and quantifying C_A accumulation in the ocean interior [*Sabine and other*, 2004; *Álvarez et al.*, 2009; *Sabine et al.*, 2010] rather than on the transport of C_A into the ocean interior. The observationally studies that have included the effects of ocean circulation generally confirm that the circulation is a dominant factor for C_A sequestration [*Matear and Hirst*, 1999; *Gruber et al.*, 2009]. Hence, to understand and quantify the surface to interior ocean pathways of C_A, accounting for interior ocean circulation is essential for the interpretation of observed interior distributions and response of ocean models [*Graven et al.*, 2012]. This is illustrated by the work of *Levy et al.* [2013], who used the approach of *Sallee et al.* [2012], to show that in the Southern Ocean, these surface to interior pathways are dominated

by a complex pattern of subduction and reventilation regions, which have well-defined locations where C_A is transported into the ocean interior.

Khatiwala et al. [2013] showed that for a wide range of models, the distribution and magnitude of C_A are broadly consistent with the observed distribution. The Green function method [e.g., *Mikaloff Fletcher et al.*, 2006; *Khatiwala et al.*, 2013] can quantify the annual mean uptake and accumulation of C_A in the ocean; however, the method assumes a mean ocean circulation and air-sea gas exchange. Therefore, it cannot elucidate the dynamical processes that result in water mass accumulation and redistribution of C_A in the ocean interior, which is important in regions such as the Southern Ocean [*Lenton et al.*, 2013]. In the Southern Ocean, the seasonal cycle may exerts a strong control on the oceans ability to sequester and redistribute C_A into the ocean interior. The inability of the Green function method to correctly represent seasonality, but still capture the large-scale C_A accumulation, suggests that the seasonal processes are not important to the oceanic transport of C_A into the ocean interior. In this context the questions we will investigate are the following: (1) How important are the relative roles of the mean, seasonal cycles, surface fluxes, and diffusion with respect to each other for the C_A distribution in the ocean? (2) Can we unravel and understand the resulting circulation using the aforementioned processes?

The oceanic uptake and the subsequent transport of C_A into the ocean interior are complex, and unraveling the spatially and temporal varying C_A circulation is challenging. Here we use a diagnostic developed by *Groeskamp et al.* [2014a] that uses a volumetric stream function to simplify the three-dimensional time varying (global) ocean circulation into a two-dimensional time-averaged circulation. This diagnostic separates the effect of seasonality, advection, and the trend for physically relevant combination of tracers, allowing for the redistribution and accumulation of the chosen tracers in the ocean to be explored and quantified. We apply this diagnostic to the surface referenced potential density anomaly (σ_0) and anthropogenic dissolved inorganic carbon (C_A) of the Commonwealth Scientific and Industrial Research Organisation (CSIRO) ocean biogeochemical model for the period of 1990–1999. Our diagnostic provides the ocean circulation in (C_A, σ_0) coordinates. This method is in essence a two-dimensional extension of the method used by *Iudicone et al.* [2011] but applied globally to C_A and σ_0 instead to total carbon at 30°S. This allows us to investigate the globally integrated quantities of the entire overturning circulation rather than local subduction and provides an alternative view of the ocean circulation to that of *Iudicone et al.* [2011].

By linking together the individual contributions of the circulation, seasonality, and the trend, we are able to provide new insights into the surface to interior connection of C_A. Our results demonstrate that there are globally integrated pathways which control the rate of transport of C_A into the ocean interior. Furthermore, our approach also provides a useful diagnostic that can applied to ocean models to show how they transport C_A and to elucidate how this transport may change in the future. Our diagnostic expands on previous work, providing a way to represent the three-dimensional time-varying ocean transport of C_A in a manner analogous to the global meridional overturning stream function.

2. Methods: Circulation in (C_A, σ_0) Coordinates

In this section we provide a summary of the methodology derived in *Groeskamp et al.* [2014a] and apply it to the surface referenced potential density anomaly (σ_0) and anthropogenic dissolved inorganic carbon (C_A) coordinates generated by an Ocean Biogeochemical model.

A stream function (Ψ) represents a three-dimensional time-varying ocean circulation as a two-dimensional time-averaged ocean circulation. Stream functions are a model diagnostic widely used to understand ocean circulation pathways and to quantify the associated transports. This leads to a more comprehensible projection, qualification, and interpretation of the resulting ocean circulation.

Originally, stream functions were constructed having at least one fixed x, y, or z coordinate (*Stommel* [1948], *Marotzke et al.* [1988], *Döös and Webb* [1994], *Hirst et al.* [1996], *Nurser and Lee* [2004], *Boccaletti et al.* [2005], *Nycander et al.* [2007], among others). Recently, *Zika et al.* [2012] and *Döös et al.* [2012] calculated the thermohaline stream function Ψ_{ST}, a stream function in salinity (S) and temperature (T) coordinates; two tracer coordinates that are not fixed in space and time. They calculated the component of the ocean circulation in the direction normal to the surfaces of constant S (isohalines) and T (isotherms), providing the advective component of the circulation in (S, T) coordinates. However, they did not calculate the component of the circulation in (S, T) coordinates due to the movement of isohalines and isotherms in space and time, like that

associated with a seasonal cycle. *Groeskamp et al.* [2014a] did include this effect and calculated the diathermohaline stream function Ψ^{dia}_{ST} that takes into account both the advective component and the component due to the movement of the tracers surfaces themselves—termed the local component. The local component mainly represents the effect of seasonal cycles on the (S, T) distribution. Only Ψ^{dia}_{ST} allows for a direct relationship between the circulation in (S, T) and the related fluxes of salt and heat. It is this formalism that we will use to calculate the dia carbon-density stream function $\Psi^{dia}_{C_A\sigma_0}$.

2.1. Ocean Biogeochemical Model

To illustrate the ocean circulation in (C_A, σ_0) coordinates, we apply the methodology of *Groeskamp et al.* [2014a] to the monthly mean output from the prognostic CSIRO Biogeochemical Ocean General Circulation Models, focussed on a short period of this simulation (1990–1999). This model has been used to investigate carbon cycling in the ocean and ocean response of atmospheric forcing in many studies [*Lenton et al.*, 2013; *Wanninkhof et al.*, 2013; *Sarma et al.*, 2013; *Schuster et al.*, 2013]. Here we present a short description of the model; for a more comprehensive description of this model the reader is directed to *Lenton and Matear* [2007] and *Matear and Lenton* [2008]. The ocean physical model was based on the *Z* coordinate Modular Ocean Model (MOM) version 3 [*Pacanowski and Griffies*, 1998]. The model grid has a horizontal resolution of 0.94°N-S and 1.9°E-W at the equator, with a tapering of longitude as a function of the cosine of latitude and 31 nonregular vertical levels, of which 15 levels in the upper 500 m. This model is not eddy resolving; instead, the GM-scheme was implemented to represent the effects of eddies [*Gent and McWilliams*, 1990; *Gent et al.*, 1995]. Our biogeochemical model predicted dissolved inorganic carbon (DIC), alkalinity, oxygen, and phosphate, with phosphate as the limiting nutrient.

The model was initialized with the values of preindustrial DIC and alkalinity from GLobal Ocean Data Analysis Project (GLODAP) [*Key et al.*, 2004] and temperature and salinity fields from the World Ocean Atlas [*Conkright et al.*, 2002] in accordance with the protocols of the Northern Ocean Carbon Exchange Study (NOCES)/Ocean Carbon Model Inter-comparison Project 3 (OCMIP3) (O. Aumont et al., NOCES Project: Inter-annual HOWTO, 2004, http://www.ipsl.jussieu.fr/OCMIP/time3/simulations/NOCES/HOWTO-NOCES.html). The protocols of NOCES were designed to simulate variability in global biogeochemical ocean models on interannual to interdecadal timescales. The model was forced with daily wind stress, heat, and freshwater fluxes from National Centers for Environmental Prediction Reanalysis 1 (NCEP-R1) [*Kalnay et al.*, 1996]. As the model was not coupled to a sea-ice model, the effects of sea-ice on heat and freshwater fluxes were accounted for by the use of NCEP-R1 forcing that does contain sea ice. C_A is calculated as the difference between two tracers of DIC, one that sees a (preindustrial) atmospheric value of 280 ppm and a second tracer that sees the observed atmospheric pCO_2 history since 1837 [*Le Quéré et al.*, 2014]. In this way the biological impact on the annual and seasonal variability is removed, but the impact of interannual and longer-time ocean circulation variability remains. For our calculations in (C_A, σ_0) coordinate we used discrete grid with $\Delta\sigma_0 = 0.03$ kg m^{-3} and $\Delta C_A = 0.25$ mmol m^{-3}.

Previous studies have shown that the model provides a reasonable simulation of the real ocean. In the North Atlantic the simulated Atlantic meridional overturning stream function of 16 sverdrup (Sv) is in very good agreement with observations collected at the Research with Adaptive Particle Imaging Detectors time series site at 26.5 N [*Buckley and Marshall*, 2016] and state-of-the-art model simulations [*Danabasoglu et al.*, 2016]. In the Southern Ocean, where limited observations exist, the strength of the Meridional Overturning Circulation (MOC) is consistent with current state-of-the-art model simulations [*Farneti et al.*, 2015].

The seasonal response of mixing also has been assessed. The structure of the summer and mixed layer depths is comparable to those estimated from Monthly Isopycnal/Mixed-layer Ocean Climatology (MIMOC) (Figure 1) based on a 0.125 kg m^{-3} density criteria [*Schmidtko et al.*, 2013]. At low latitudes the model has good agreement with observations. In the higher-latitude ocean, the summer mixed layer depth is in agreement with observations. During the winter there is very good agreement between the spatial structure of the winter mixed layer, but the model mixed layer depth is deeper than observed. However, in the Southern Ocean we see that the simulated mixed layers depths lie well with in the range of state-of-the-art ocean models [*Downes et al.*, 2015].

The modeled global ocean uptake of C_A of 1.79 Pg C_A yr^{-1} for the 1990s is comparable to recent estimates from other models and observations [*McNeil and Matear*, 2013; *Wanninkhof et al.*, 2013]. In key areas of anthropogenic uptake such as the Southern Ocean the model captures well both the large-scale uptake and transport of C_A into the ocean interior and the seasonal cycle of dissolved inorganic carbon in the upper

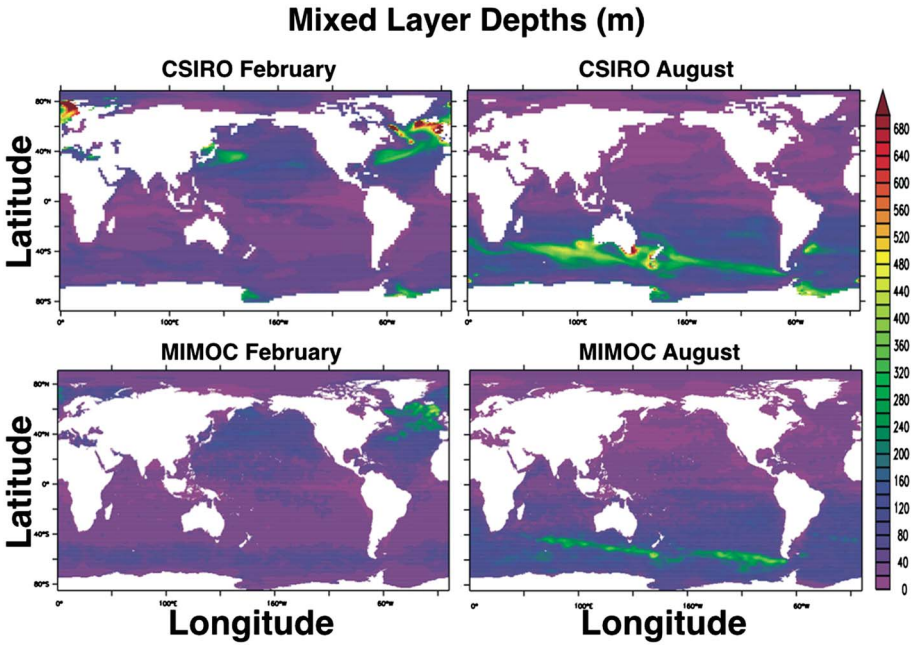

Figure 1. (top) Mixed Layer Depth for the CSIRO Division Biogeochemistry (BGC) Ocean General Circulation Models (OGCM) and (bottom) MIMOC, for (left) February and (right) August.

ocean [*Lenton et al.*, 2013]. The structure and magnitude of C_A uptake from the model simulation agrees very well with GLODAP observations [*Sabine et al.*, 2005] for the year 1995, except for a minor difference in the North Atlantic where observations suggests a larger uptake in the eastern North Atlantic (Figure 2). This difference maybe due to either the sporadic deep convective mixing that occurs in this region [*Vage et al.*, 2009] that is not simulated in this model or the limited observations of anthropogenic carbon in this region.

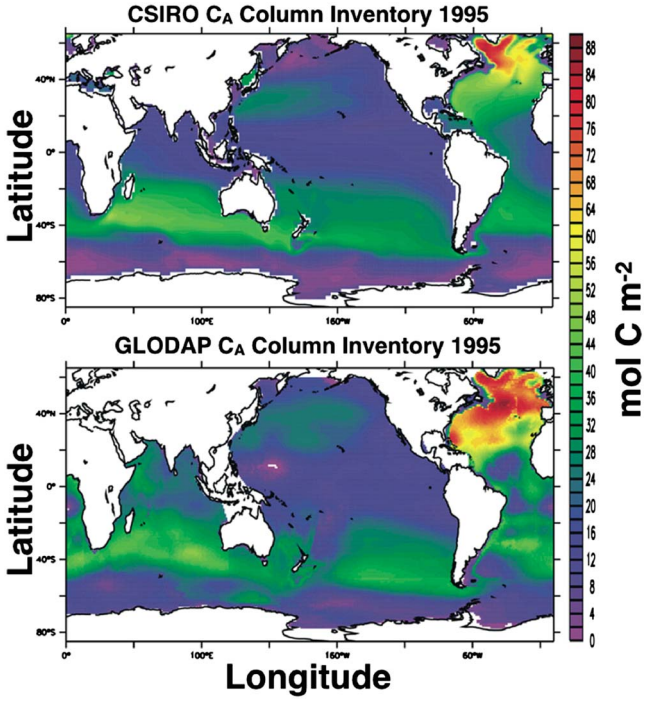

Figure 2. Column inventory of C_A (mol C_A m^{-2}) for the year 1995 for the (top) CSIRO Division BGC OGCM and (bottom) GLODAP [*Sabine et al.*, 2005].

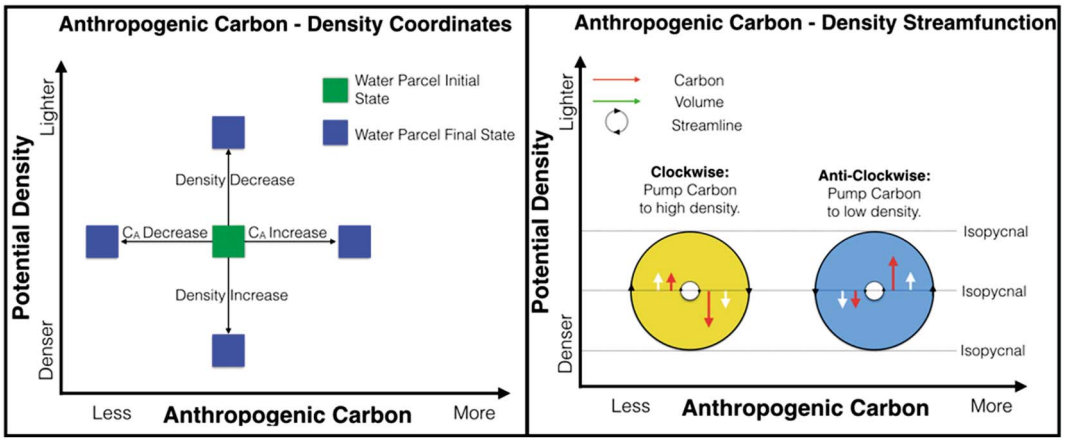

Figure 3. (a) Schematic of the changes in a water-parcel properties that are required for it to be able to move in particular directions in (C_A, σ_0) coordinates. (b) Schematic of how a closed circulation in (C_A, σ_0) coordinates can lead to redistribution of C_A to either higher or lower densities. The volume transports (white arrows) toward denser and lighter water is exactly the same, such that, integrated over one isopycnal, there is no net volume transport. However, the concentration of C_A at those locations where the volume transport takes place is not the same (red arrows). This results in a net transport of C_A. The direction of rotation of the cell, determines if this net transport is toward higher densities or lower densities.

Our model simulations of anthropogenic uptake also lie well within the range of current ocean biogeochemical models [*Khatiwala et al.*, 2013].

2.2. Dia Carbon-Density Circulation

Here we provide mathematical details on how to construct the stream functions. A more conceptual explanation is provided from equation (8) and onward.

To construct a stream function, a nondivergent two-dimensional velocity field is required. In our study, the two-dimensional flow field is given by the volume transport in (C_A, σ_0) coordinates. The C_A and σ_0 values of a fluid parcel determines its position in (C_A, σ_0) coordinates. To change this position and obtain a volume transport in (C_A, σ_0) coordinates, a change in C_A or σ_0 is required (Figure 3a), as described by their conservation equations:

$$\frac{D\sigma_0}{Dt} = \frac{\partial \sigma_0}{\partial t} + \left(\mathbf{u}_m + \mathbf{u}_{GM}\right) \cdot \nabla \sigma_0 = f_{\sigma_0} + d_{\sigma_0} + n_{\sigma_0}, \tag{1}$$

$$\frac{DC_A}{Dt} = \frac{\partial C_A}{\partial t} + \left(\mathbf{u}_m + \mathbf{u}_{GM}\right) \cdot \nabla C_A = f_{C_A} + d_{C_A}. \tag{2}$$

Here $\mathbf{u}_m = (u_m, v_m, w_m)$ and $\mathbf{u}_{GM} = (u_{GM}, v_{GM}, w_{GM})$ are the Eulerian mean and eddy velocity vectors (m s^{-1}), respectively. f_{σ_0} and f_{C_A} are the air-sea fluxes of σ_0 (kg m^{-3} s^{-1}) and C_A (C_A s^{-1}), respectively, and d_{σ_0} and d_{C_A} are the diffusive fluxes (by mixing) of σ_0, and C_A, respectively. n_{σ_0} are changes in σ_0 due to nonlinearities in the equation of state. We have not included a biological term in equation (2) as this term is removed through the definition of C_A. The ocean model diffuses DIC and not C_A, such that d_{C_A} is not a standard tracer diffusive flux term but instead some function of the difference in DIC diffusion between the two tracers. Equations (1) and (2) show that the total change in σ_0 or C_A due to the forcing terms on the right-hand side leads to either a local change $(\partial \sigma_0 / \partial t)$ or an advective change $\left(\left(\mathbf{u}_m + \mathbf{u}_{GM}\right) \cdot \nabla \sigma_0\right)$.

The nondivergent component of the volume transport in (C_A, σ_0) coordinates as a result of the σ_0 and C_A fluxes can now be represented by the dia carbon-density stream function $\Psi^{dia}_{C_A \sigma_0}$. Following *Groeskamp et al.* [2014a, 2014b], the expression for the stream function is given by

$$\Psi^{dia}_{C_A \sigma_0}(C_A, \sigma_0) = \frac{1}{\Delta t} \int_t^{t+\Delta t} \int_{\sigma_0' \le \sigma_0|_{C_A}} \frac{1}{|\nabla C_A|} \left[\frac{DC_A}{Dt} - \tau^{trend}_{C_A}\right] dA dt \tag{3}$$

$$= -\frac{1}{\Delta t} \int_t^{t+\Delta t} \int_{C_A' \le C_A|_{\sigma_0}} \frac{1}{|\nabla \sigma_0|} \left[\frac{D\sigma_0}{Dt} - \tau^{trend}_{\sigma_0}\right] dA dt \tag{4}$$

Here $\int_{C_A \le C_A|_{\sigma_0}} (\ldots) dA$ is the area integral over all C_A' smaller than or equal to C_A, on a surface of constant σ_0. $\int_{\sigma_0' \le \sigma_0|_{C_A}} (\ldots) dA$ is the area integral over all σ_0' smaller than or equal to σ_0, on a surface of constant C_A, and $1/\Delta t \int_t^{t+\Delta t} (\ldots) dt$ is a time average over time period Δt.

The stream function can only be constructed from an exact non-divergent flow. As a net change in C_A and σ_0 over time leads to a divergent flow in (C_A, σ_0) coordinates, we have included trend terms ($\tau_{C_A}^{\text{trend}}$ and $\tau_{\sigma_0}^{\text{trend}}$, equations (3) and (4)) for compensation. The trends emerge from the tendency terms $\partial\sigma_0/\partial t$ and $\partial C_A/\partial t$ and are driven by trend in air-sea fluxes. Here the trends are calculated as the difference between the last and initial value, given by

$$\tau_{C_A}^{\text{trend}} = \frac{C_A(t+\Delta t) - C_A(t)}{\Delta t}, \text{and} \tau_{\sigma_0}^{\text{trend}} = \frac{\sigma_0(t+\Delta t) - \sigma_0(t)}{\Delta t} \tag{5}$$

The cyclical components contained in the tendency terms are accounted for in equations (3) and (4). For a Boussinesq ocean $\nabla \cdot \mathbf{u}_{GM} = \nabla \cdot \mathbf{u}_m = 0$ by construction, leading to an exact nondivergent flow in both Cartesian and (C_A, σ_0) coordinates and thus requires no correction.

For notation purposes let us replace $\int_{\sigma_0' \le \sigma_0|_{C_A}} (\ldots) dA$ by $\int [\ldots]$ and inserting equation (2) into equation (3) to obtain

$$\Psi_{C_A\sigma_0}^{\text{dia}} = \underbrace{\int \left[\frac{1}{|\nabla C_A|} \left(\frac{\partial C_A}{\partial t} - \tau_{C_A}^{\text{trend}} \right) \right]}_{\Psi_{C_A\sigma_0}^{\text{loc}}} + \underbrace{\int \left[\mathbf{u}_m \cdot \frac{\nabla C_A}{|\nabla C_A|} \right]}_{\Psi_{C_A\sigma_0}^{\text{mean}}} + \underbrace{\int \left[\mathbf{u}_{GM} \cdot \frac{\nabla C_A}{|\nabla C_A|} \right]}_{\Psi_{C_A\sigma_0}^{\text{eddy}}} \tag{6}$$

which can be written as

$$\Psi_{C_A\sigma_0}^{\text{dia}} + \underbrace{\int \left[\frac{\tau_{C_A}^{\text{trend}}}{|\nabla C_A|} \right]}_{T_{C_A}} = \underbrace{\int \left[\frac{f_{C_A}}{|\nabla C_A|} \right]}_{F_{C_A}} + \underbrace{\int \left[\frac{d_{C_A}}{|\nabla C_A|} \right]}_{D_{C_A}} \tag{7}$$

For further details on the mathematics and numerical implementation of stream functions similar to equations (3)–(7), we refer the reader to *Ferrari and Ferreira* [2011], *Zika et al.* [2012], *Döös et al.* [2012], *Kjellsson et al.* [2013], *Groeskamp et al.* [2014a, 2014b], *Hieronymus et al.* [2014], and *Laliberté et al.* [2015]. We will continue with a more conceptual explanation using a short-hand notation of equation (7):

$$\Psi_{C_A\sigma_0}^{\text{dia}} = \Psi_{C_A\sigma_0}^{\text{loc}} + \Psi_{C_A\sigma_0}^{\text{mean}} + \Psi_{C_A\sigma_0}^{\text{eddy}} = F_{C_A} + D_{C_A} - T_{C_A} = -\left[F_{\sigma_0} + D_{\sigma_0} - T_{\sigma_0} \right] \tag{8}$$

Here F_{C_A}, D_{C_A}, and T_{C_A} (F_{σ_0}, D_{σ_0}, and T_{σ_0}) are the fluxes of C_A (σ_0) due to air-sea interaction, diffusive fluxes, and the trend, respectively. $\Psi_{C_A\sigma_0}^{\text{adv}} = \Psi_{C_A\sigma_0}^{\text{mean}} + \Psi_{C_A\sigma_0}^{\text{eddy}}$ is the advective carbon-density stream function and represents the advective component of the ocean circulation that is in the direction normal to C_A and σ_0 isosurfaces. Hence, it is the component of the ocean circulation that is related to a circulation in both geographical coordinates and (C_A, σ_0) coordinates. We have split $\Psi_{C_A\sigma_0}^{\text{adv}}$ into a contribution from the Eulerian mean velocity $\Psi_{C_A\sigma_0}^{\text{mean}}$ and the parameterized eddy-induced velocity $\Psi_{C_A\sigma_0}^{\text{eddy}}$. Note that advection of fluid parcels that do not experience a change in C_A or σ_0 do not show up in (C_A, σ_0) coordinates.

$\Psi_{C_A\sigma_0}^{\text{loc}}$ is the local carbon-density stream function and represents movement of the isosurfaces in the direction normal to itself, due to local changes of C_A and σ_0 that leads to changes in the volume distribution of the ocean in (C_A, σ_0) coordinates, without a net displacement of volume in geographical coordinates. The changes in (C_A, σ_0) coordinates can either be permanent, leading to a dia carbon-density trend, or they can be cyclical. The permanent changes in (C_A, σ_0) coordinates that lead to a dia carbon-density trend (T_{σ_0} and T_{C_A}) are taken into account on the right-hand side of equation (8). With cyclical we refer to a succession of changes of the C_A and σ_0 values of the fluid parcel over time (and related movement of the isosurfaces), such that initial and final value of C_A and σ_0 are similar, over the considered period of time Δt. Over Δt, the cyclical redistribution of the ocean's volume in (C_A, σ_0) coordinates leads to a nondivergent circulation in (C_A, σ_0) coordinates, represented by $\Psi_{C_A\sigma_0}^{\text{loc}}$.

When analyzing the time-averaged circulation over the 10 years considered, the main source for the local stream function are seasonal cycles of buoyancy and C_A fluxes. The dia carbon-density trend (T_{σ_0} and T_{C_A}) may be due to incomplete cycles within the considered time period (e.g., an El Niño) or longer-term changes, as for example, global warming or an increase in atmospheric C_A and related air-sea fluxes of C_A. The dominant features found in both the dia carbon-density trend and local carbon-density stream function depend on the considered time period (10 years) and the sample resolution within that period (1 month).

$\Psi^{dia}_{C_A\sigma_0}$ represents the net transport through C_A and σ_0 surfaces (hence the prefix "dia"). The transport through a surface can be calculated as the difference between the transport of fluid in the direction normal to the surface as represented by $\Psi^{adv}_{C_A\sigma_0}$ and transport due to the movement of the surface in the direction normal to itself as represented by $\Psi^{loc}_{C_A\sigma_0}$. Therefore, $\Psi^{dia}_{C_A\sigma_0} = \Psi^{adv}_{C_A\sigma_0} + \Psi^{loc}_{C_A\sigma_0}$ and, unlike $\Psi^{adv}_{C_A\sigma_0}$ and $\Psi^{loc}_{C_A\sigma_0}$ itself, is directly related to the fluxes on the right-hand side of equation (8).

Both the circulation (represented by the stream functions $\Psi^{dia}_{C_A\sigma_0}$, $\Psi^{adv}_{C_A\sigma_0}$, or $\Psi^{loc}_{C_A\sigma_0}$) and the diffusive fluxes do not lead to a net change in the C_A inventory. This is because the overturning is nondivergent by definition, while the local changes are nondivergent by construction, even though both are superimposed on top of a changing C_A and σ_0 distribution (represented by the trend). Only surface fluxes lead to a net increase in C_A. The method we use here therefore reveals how the net input of C_A by surface fluxes is redistributed by the circulation and the diffusive fluxes, leading to the observed distribution of the trend. In this process we are also able to separate the effects of advection from that by cyclical motion of isopycnals (mostly due to seasonal cycles).

To interpret the circulation cells of the stream function in (C_A, σ_0) coordinates, we consider a circulation cell that is rotating in an clockwise manner (i.e., positive cell in Figure 3b). The related transport across an isopycnal surface (horizontal line) has a net transport of C_A to higher σ_0, because the C_A that is transported to higher σ_0 always exceeds the C_A transport to lower σ_0. In contrast, the anticlockwise circulation cells (i.e., negative cell in Figure 3b) leads to a net transport of C_A toward lower σ_0.

2.3. Diapycnal Transports and Accumulation

Although the circulation as represented in the carbon-density stream functions do not change the net amount of C_A in the ocean, they do change the distribution. The amount of C_A which is redistributed from one σ_0 range to another by the circulation cells can be calculated. First, we calculate the diapycnal C_A transport as a result of the dia carbon-density stream function $e^{dia}_{C_A}(\sigma_0)$, surface fluxes $e^{F}_{C_A}(\sigma_0)$, diffusive fluxes $e^{D}_{C_A}(\sigma_0)$, and trend $e^{T}_{C_A}(\sigma_0)$ by integrating the C_A transport across an isopycnal over the entire global domain

$$\underbrace{\int_{\sigma_0} C_A \, d\Psi^{dia}_{C_A\sigma_0}}_{e^{dia}_{C_A}(\sigma_0)} + \underbrace{\int_{\sigma_0} C_A \, dT_{C_A}}_{e^{T}_{C_A}(\sigma_0)} = \underbrace{\int_{\sigma_0} C_A \, dF_{C_A}}_{e^{F}_{F_{C_A}}(\sigma_0)} + \underbrace{\int_{\sigma_0} C_A \, dD_{C_A}}_{e^{D}_{C_A}(\sigma_0)} \tag{9}$$

Here $\int_{\sigma_0} d\Psi^{dia}_{C_A\sigma_0}$ integrates the diapycnal volume transport ($d\Psi^{dia}_{C_A\sigma_0}$; in $m^3\ s^{-1}$) multiplied by the tracer concentration C_A (in mmol m^{-3}), along the isopycnal with value σ_0. Likewise for the volume transport resulting from dF_{C_A}, dD_{C_A}, and dT_{C_A}. If the diapycnal transport of C_A is positive, it indicates a net transport of C_A from lighter to denser water and is associated with a clockwise-rotating cell. If the diapycnal transport of C_A is negative, it indicates a net transport of C_A from denser to lighter water and is associated with an anticlockwise rotating cell. By taking the derivative of the diapycnal transport of C_A, we can calculate the accumulation of C_A for a particular σ_0, leaving

$$\underbrace{-\frac{\partial e^{dia}_{C_A}}{\partial \sigma_0}}_{a^{dia}_{C_A}} \underbrace{-\frac{\partial e^{T}_{C_A}}{\partial \sigma_0}}_{a^{T}_{C_A}} = \underbrace{-\frac{\partial e^{F}_{C_A}}{\partial \sigma_0}}_{a^{F}_{C_A}} \underbrace{-\frac{\partial e^{D}_{C_A}}{\partial \sigma_0}}_{a^{D}_{C_A}} \tag{10}$$

The accumulation due to the diffusive fluxes ($a^{D}_{C_A}$ in Pg C_A y^{-1} (kg m^{-3})$^{-1}$) is calculated as a residual and is given by

$$a^{D}_{C_A} = a^{dia}_{C_A} + a^{T}_{C_A} - a^{F}_{C_A} \tag{11}$$

A positive (negative) accumulation indicates an increase (decrease) in C_A for that particular density range.

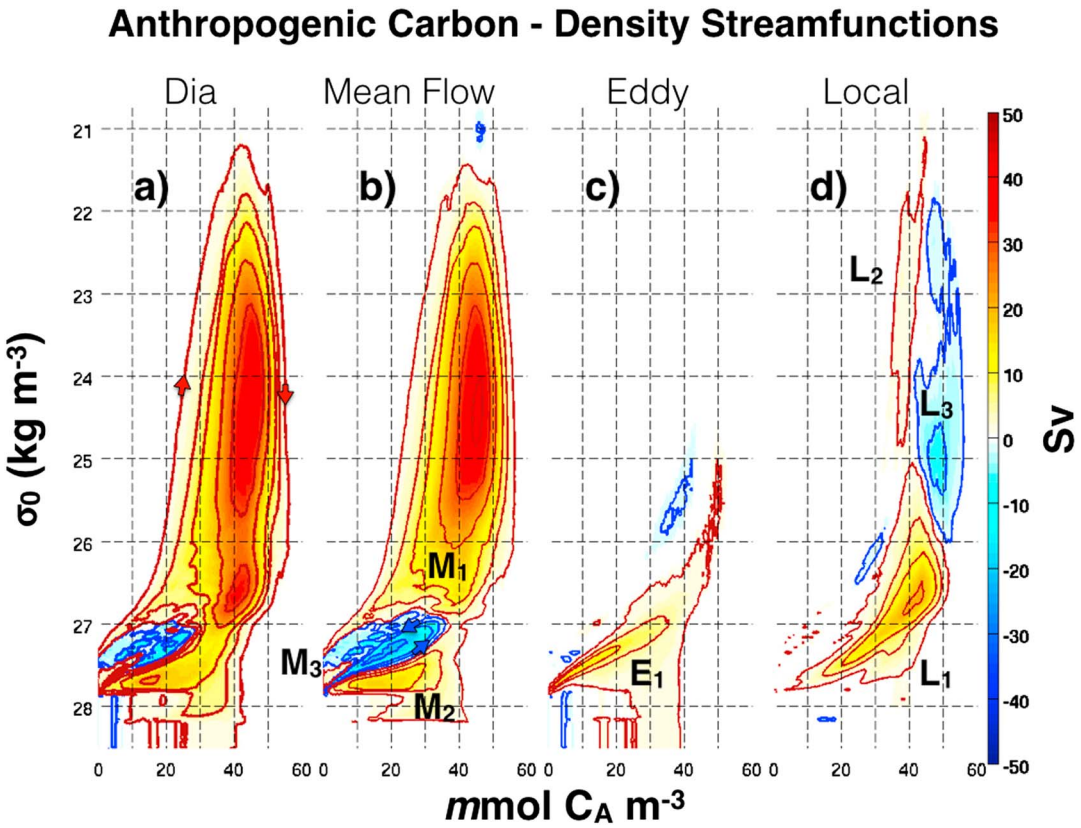

Figure 4. The ocean circulation in (C_A, σ_0) coordinates decomposed into the (a) dia, (b) Eulerian mean, (c) eddy-induced, and (d) local carbon-density stream function. Positive cells (red/yellow) rotate clockwise and produce a net transport of C_A to denser water. Negative cells (blue) rotate anticlockwise and produce a net transport of C_A to lighter water. Transports are provided in Sverdrups (1 Sv = 10^6 m^3 s^{-1}). Cell names (as used in the text) are indicated by M_1, M_2, etc.

3. Results: The Carbon-Density Stream Functions

We apply our diagnostic to the model simulation of C_A to determine the carbon-density stream function and trend. From the model simulations we compute the ocean circulation in (C_A, σ_0) coordinates, represented by, 1) the Dia carbon-density stream function $\Psi^{dia}_{C_A\sigma_0}$ (Figure 4a), 2) the Eulerian mean carbon-density stream function $\Psi^{mean}_{C_A\sigma_0}$ (Figure 4b), 3) the Eddy carbon-density stream function $\Psi^{eddy}_{C_A\sigma_0}$ (Figure 4c) and 4) the Local carbon-density stream function $\Psi^{loc}_{C_A\sigma_0}$ (Figure 4d).

To aid the interpretation of the carbon-density stream functions we will relate them to a geographical location using scatter plots (Figure 5). These plots are color-coded according to either their horizontal location or their depth. As a result, it is possible to relate certain areas in (C_A, σ_0) coordinates to particular geographical locations. For example, we find that the ocean's volume with C_A>25 mmol m^{-3} and σ_0< 26.8 kg m^{-3} is in the upper 200 m (green dots; Figure 5a) in the subtropics of the main ocean basins (Figure 5b). Only at high latitudes (Southern Ocean, North Atlantic) do we find σ_0>26.8 kg m^{-3} at the surface (green dots; Figure 5b). For the ocean's volume at depths greater than or equal to 1000 m we generally find C_A <20 mmol m^{-3} that decreases with increasing depth (Figure 5). We use Figure 6 to indicate the geographical position of the different circulation cells of the carbon-density stream functions.

3.1. Dia Carbon-Density Stream Function

The dia carbon-density stream function $\Psi^{dia}_{C_A\sigma_0}$ is dominated by a large clockwise rotating cell (red cell; Figure 4a), reflecting C_A transport to higher σ_0. There is also an anti-clockwise cell (blue cell) for σ_0>27 kg m^{-3} at ocean mid-depths. Most of the signal in $\Psi^{dia}_{C_A\sigma_0}$ is due to $\Psi^{mean}_{C_A\sigma_0}$, representing the Eulerian mean flow (Figure 4). Significant effects by eddies $\Psi^{eddy}_{C_A\sigma_0}$ are limited to the Southern Ocean region (Figures 5 and 6b). $\Psi^{loc}_{C_A\sigma_0}$, the effects of seasonality, is generally larger than those due to eddies $\Psi^{eddy}_{C_A\sigma_0}$, and has a significant

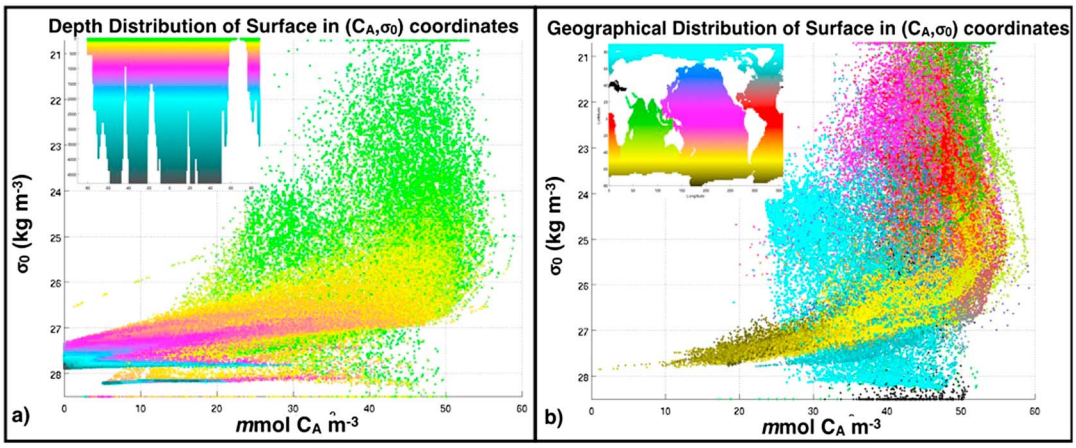

Figure 5. Projection of the σ_0 and C_A values for a particular geographical location and depth in (C_A, σ_0) coordinates. (a) The global σ_0 and C_A distribution with depth in (C_A, σ_0) coordinates. Here the color indicates depths, according to the color distribution of the inset. (b) The spatial σ_0 and C_A distribution at the surface in (C_A, σ_0) coordinates. Here the color indicates its location at the ocean surface, according to the color distribution of the inset. Hence, these figures provide information about the spatial location of the circulation cells of the carbon-density stream functions.

contribution to the total $\Psi^{dia}_{C_A\sigma_0}$ (Figure 4). We will further unravel the details of $\Psi^{dia}_{C_A\sigma_0}$ by discussing its decomposition into $\Psi^{mean}_{C_A\sigma_0}$, $\Psi^{eddy}_{C_A\sigma_0}$, and $\Psi^{loc}_{C_A\sigma_0}$.

3.2. The Mean Flow and Eddy Carbon-Density Stream Function

Here we will discuss the cells present in the mean and eddy carbon-density stream functions. We use abbreviations for the different ocean water masses, as defined by a particular σ_0 range (Table 1).

3.2.1. The M_1 Circulation Cell

The entire M_1 cell is defined as the circulation for $\sigma_0 < 27$ kg m^{-3} and covers the area in (C_A, σ_0) coordinates that corresponds to the geographical location of the subtropical gyres, thermocline water (TW), and sub-Antarctic mode water (SAMW) and reflects the redistribution C_A linked to the upper limb of the meridional overturning circulation (Figures 5 and 6). M_1 results from subtropical gyres transporting light water from the equator toward the poles at the surface of the ocean. The poleward densification of the surface water in combination with Ekman pumping transfers C_A into denser water. The subducted water moves equatorward

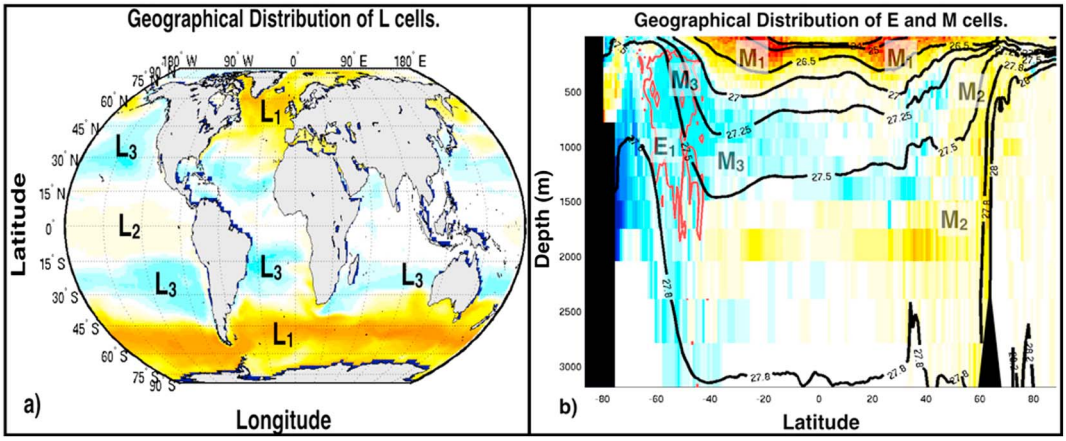

Figure 6. (a) The geographical position of circulation cells present in $\Psi^{loc}_{C_A\sigma_0}$, assuming that they are mainly located at the surface of the ocean. To do so, we (1) select a particular σ_0 and C_A combination, (2) find the associated $\Psi^{loc}_{C_A\sigma_0}$ value, and (3) represent this value at the surface of the ocean that has the same σ_0 and C_A combination. (b) The geographical position of circulation cells present in $\Psi^{mean}_{C_A\sigma_0}$ and $\Psi^{eddy}_{C_A\sigma_0}$ (see Figure 4). We apply steps (1)–(3) to cells M_1, M_2, M_3 and E_1 but in three dimensions rather than only to the surface. Then the result averaged in the meridional direction. The magnitude has no physical meaning in Figure 6b and is therefore scaled to provide an indication of the geographical distribution of these circulation cells. The location of E_1 is given by the red contours.

Table 1. Definition of Water-Masses in This Study[a]

Water Mass	Abbreviation	σ_0 Class	Trend	Air-Sea	Mixing	$\Psi^{dia}_{C_A\sigma_0}$	$\Psi^{mean}_{C_A\sigma_0}$	$\Psi^{eddy}_{C_A\sigma_0}$	$\Psi^{loc}_{C_A\sigma_0}$
		kg m^{-3}				Pg C_A y^{-1}			
Thermocline water	TW	< 26.5	0.46 (26%)	0.96	−0.71	−0.21	−0.12	−0.01	−0.08
Sub-Antarctic Mode water	SAMW	26.5–27.0	0.50 (28%)	0.30	0.30	0.11	0.13	−0.02	0.00
Antarctic Intermediate Water	AAIW	27.0–27.5	0.52 (29%)	0.38	0.14	0.00	0.00	−0.02	0.02
Circumpolar Deep water	CDW	27.5–27.75[b]	0.12 (7%)	0.10	−0.04	−0.08	−0.15	0.02	0.04
North Atlantic Deep Water	NADW	27.75–28[b]	0.13 (7%)	0.01	0.24	0.14	0.11	0.02	0.01
Antarctic Bottom water	AABW	28–bottom[b]	0.06 (3%)	0.01	0.08	0.03	0.03	0.00	0.00
Total			1.79	1.76	0.01	−0.01	0.00	−0.01	−0.01

[a]Water mass names, abbreviations, and definition according to a σ_0 range. For each water mass we calculate the total accumulated C_A (equation (10)) due to the trend, air sea fluxes, and mixing and the total, mean flow, eddy, and local stream functions. The total global trend and surface fluxes sum to prescribed values (within rounding errors). The sum of the accumulation by mixing and stream functions are by definition zero (within rounding errors) as they redistribute C_A and do not destroy or create C_A.

[b]At large depth greater than 1000 m, σ_0 surfaces are no longer aligned with the ocean's preferred mixing direction. The use of σ_0 will then lead to fictious diapycnal mixing, also known as the Veronis effect [*Veronis*, 1975]. We therefore need to be careful with interpretations related to CDW, NADW, and AABW as they may partly be below 1000 m depth.

along isopycnals while mixing with surrounding water that has a lower C_A concentration, decreasing the C_A value. Upwelling near the equator and subsequent exposure to the surface will restore the original C_A and σ_0 values. The entire M_1 cell has a globally integrated transport of 42 Sv transporting a net of 0.24 Pg C_A yr^{-1} from σ_0 = 21.0–24.8 kg m^{-3} to σ_0 = 24.8–27.1 kg m^{-3} (Figure 7 and Table 2).

The inner part of M_1, for which $\Psi^{mean}_{C_A\sigma_0} \geq 20$ Sv and $\sigma_0 < 26$ kg m^{-3}, is located entirely in the upper 300 m of the water column and confined to the subtropical gyres. It has a globally integrated transport of 22 Sv and 0.19 Pg C_A yr^{-1} from the surface toward the subsurface boundary of the gyres.

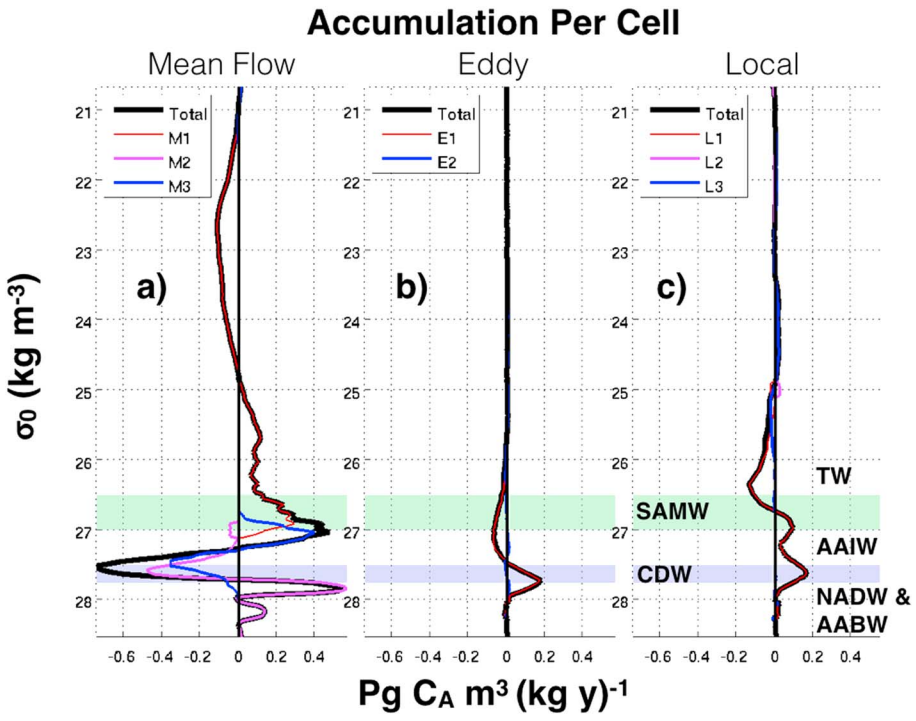

Figure 7. (a) The redistribution of C_A for each density class due to the cells $\Psi^{mean}_{C_A\sigma_0}$ as defined in Figure 4 and based on equation (10). (b and c) The same for the cells of $\Psi^{eddy}_{C_A\sigma_0}$ and $\Psi^{loc}_{C_A\sigma_0}$, respectively. The amount of C_A transported by these cells is given in Table 2. The different color shading indicate the σ_0 range of the different water masses as indicated in Figure 7c, and defined by Table 1. We used $\Delta\sigma_0 = 0.03$ kg m^{-3} and $\Delta C_A = 0.25$ mmol m^{-3}. The accumulation rates are smoothed using a running mean over 3 points.

Table 2. The Quantification of the Redistribution of C_A by the Circulation[a]

Cell	Transport (Pg C_A yr^{-1})	Transport Max $\left(\left\|\Psi^{dia}_{C_A\sigma_0}\right\|\right)$	From σ_0 Class (kg m^{-3})	To σ_0 Class (kg m^{-3})
	(% of M_1)	10^6 m^3 s^{-1}		
M_1	0.24 (100%)	42	21.0–24.8 (Surface of subtropical gyre)	24.8–27.1 (Bottom of subtropical gyre and SAMW)
M_2	0.15 (63%)	17	26.9–27.7 (Shallow North Atlantic)	27.7–28.3 (Deep North Atlantic)
M_3	0.12 (50%)	24	27.3–27.9 (CDW/AAIW)	26.7–27.3 (AAIW/SAMW)
E_1	0.05 (21%)	15	26.4–27.5 (SAMW/AAIW)	27.5–28 (CDW)
L_1	0.10 (42%)	21	25–26.7 (TW)	26.7–27.8 (SAMW/AAIW in S.O., below mixed layer in North Atlantic)
L_3	0.03 (13%)	7	24.7–26.0 (TW near surface)	23.5–24.7 (TW near surface)

[a]The first column indicates the circulation cells. The second column indicates the amount of C_A that is transported from one density class (column 4) to another (column 5) and how much this transport is compared to that by the M_1 cell. This is based on an integration of equation (10) over the density range up until the zero crossing as seen in Figure 7. The third column provides the maximum transport (in Sv) associated with this circulation. We have indicated the main water masses related to those density classes using Table 1. Transport by L_2 and E_2 are not significant and not shown.

The outer part of M_1 shows the connection between the subtropical gyres and subduction of SAMW. This cell has outcropping isopycnals that allow subduction to depths up to 500 m (e.g., $\sigma_0 = 27.0$ kg m^{-3}). It has a globally integrated transport of 20 Sv and 0.21 Pg C_A yr^{-1} from the subtropical gyre and TW ($\sigma_0 < 26.2$ kg m^{-3}) into density classes ($\sigma_0 = 26.2–27.0$ kg m^{-3}) related to SAMW. This suggests that a part of the TW in the subtropical gyres is transformed into SAMW. Note that the Northern Hemisphere branch of the outer loop is connected to North Atlantic Deep Water (NADW) formation sites through the cutoff at $\sigma_0 = 27.0$ kg m^{-3} and the higher end of the C_A values.

3.2.2. The M_2 Circulation Cell

The M_2 clockwise cell is largely due to the formation of NADW (Figures 5 and 6b). Cooling of TW at the surface leads to rapid densification and subsequently subduction of NADW water, with a high C_A content, into the ocean interior. The yellow patch in Figure 6b near the continental shelves of Antarctica at depths of about 500 m is also part of M_2 and is most likely related to the formation of Antarctic Bottom Water (AABW; location of red star in Figure 10). The C_A transport related to the AABW component seems small compared to the NADW formation component (Figure 7a; purple line, $\sigma_0 > 28$ kg m^{-3}, second peak versus first peak). M_2 has a globally integrated circulation of 19 Sv that subducts a net of 0.15 Pg C_A yr^{-1}, mostly from the NADW formation regions (> 45°N) at the surface in the North Atlantic ($\sigma_0 = 26.9–27.7$ kg m^{-3}) to depths between 500–2000 m ($\sigma_0 = 27.7–28.3$ kg m^{-3}) between 40°N and 70°N (Figures 7 and 6b and Table 2). The M_2 cell shows the redistribution of C_A is linked to the lower limb of the meridional overturning circulation.

3.2.3. The M_3 Circulation Cell

The M_3 anticlockwise cell leads to a net transport of C_A toward lighter densities, opposing of the general tendency of C_A transport toward denser waters. However, this circulation is still transporting C_A into the interior. The M_3 cell outcrops at the surface between 40°S and 60°S and at depths is found between 500 m and 1400 m (Figure 6b). This cell is therefore an interplay of Antarctic Intermediate Water (AAIW) with the denser Circumpolar Deep Water (CDW).

First, CDW with a low C_A concentration is upwelled to the surface. Subsequently, surface C_A and buoyancy fluxes transform CDW into AAIW and SAMW and increase the C_A concentration, while Ekman transport moves the water equatorward (Figure 4b). AAIW, with a higher C_A concentration than the denser upwelled CDW, is then subducted into the interior, hence leading to an anticlockwise circulation in (C_A, σ_0) coordinates. Mixing with surrounding water along the isopycnal will reduce the C_A concentration. To close the M_3 cell, we now require an increase in density of AAIW at depth, which we suggest is due to cabbeling (see below). The M_3 cell has a globally integrated circulation of 24 Sv with a net transport of 0.12 Pg C_A yr^{-1} from CDW water ($\sigma_0 = 27.3–27.9$ kg m^{-3}) to the lighter AAIW water and SAMW ($\sigma_0 = 26.7–27.3$ kg m^{-3}; Figure 7 and Table 2).

There is also an anticlockwise cell along the continental shelves of Antarctica that is most likely due to interaction between local shelf circulation and the cryosphere (Figure 6b). This cell seems to be related to mixing between newly subducted AABW and in situ CDW (blue star in Figure 10). However, due to its limited representation in this model, it is not further examined.

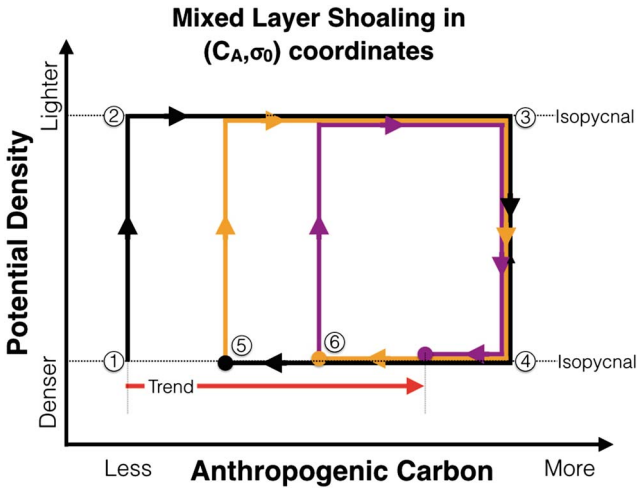

Figure 8. A schematic of mixed layer shoaling in (C_A, σ_0) coordinates and how the trend is defined. The processes are as follows: (1) we consider a fixed fluid parcel below the summer mixed layer (ML) depth. Deepening of the winter ML decreases σ_0 (1 →2) and subsequently increases C_A (2 → 3). Restratification of the ML in summer restores σ_0 to initial conditions (3 → 4). There is a slight decrease in C_A concentration by mixing due to the aforementioned processes (4 → 5). This cycle repeats multiple times over period Δt (4 → 6), leading to a net increase in C_A, i.e., the trend ($t^{rend}_{C_A}$; red arrow).

3.2.4. The E_1 Circulation Cell

The eddy-induced stream function only has one major clockwise cell (Figures 4c and 6b). The E_1 clockwise cell leads to a net transport of C_A toward higher densities at the transition between AAIW and CDW. This cell reveals eddy compensation from steepening isopycnal in the Southern Ocean due to the mean flow and is, as expected, opposing the mean flow in this area [*Marshall and Speer*, 2012]. The E_1 cell has a globally integrated circulation of 15 Sv with a net transport of 0.05 Pg C_A yr^{-1} from the upper boundary of AAIW (σ_0 = 26.4–27.5 kg m^{-3}) to CDW (σ_0 = 27.5–28 kg m^{-3}; Figure 7 and Table 2). It shows that eddy transport has a significant impact on the C_A transport in the Southern Ocean.

In the Southern Ocean, the net diapyncal transport, analyzed from the velocity field (left-hand side (LHS) of equation (8)), is the superposition of the M_3 cell (24 Sv) and opposing E_1 (15 Sv), suggesting densification of 9 Sv of AAIW. Thermodynamics (LHS of equation (8)) then suggest that at this depth this has to be due to densification upon mixing, i.e., cabbeling [*McDougall*, 1987]. This compares well to AAIW formation found in a modeling study by *Iudicone et al.* [2008a, Figure 15] and is supported by recent modeling [*Nycander et al.*, 2015] and observational based studies [*Groeskamp et al.*, 2016], which showed that cabbeling is an essential process for the formation and densification of AAIW.

3.3. Local Carbon-Density Stream Function

The local stream function $\Psi^{loc}_{C_A\sigma_0}$ represents the globally integrated circulation in (C_A, σ_0) coordinates due to cyclical motions of isosurfaces of C_A and σ_0 in the model. Cyclical motion is mainly due to seasonal cycles in surface C_A and σ_0 fluxes and therefore mainly occurs near the surface. In $\Psi^{loc}_{C_A\sigma_0}$ we distinguish three separate circulation cells (L_1, L_2, and L_3; Figure 4c) that have a clear geographical separation (Figures 5b and 6a). Cell L_2 and L_3 are confined to approximately the upper 75 m, while L_1 circulates much deeper into the ocean (up to 500 m).

The L_1 cell is confined to the middle and high latitudes of the Southern, North Atlantic, and North Pacific Oceans (Figure 6a) but is most pronounced in the Southern Ocean. The L_1 cell is a result of seasonal changes of the mixed layer depth. The mixed layer has a high C_A concentration and is lighter compared to the underlying water. In winter, deepening of the mixed layer decreases the upper ocean density with a subsequent increase in C_A due to mixing. The reverse happens in summer when the mixed layer shoals. This results in a clockwise cell in (C_A, σ_0) coordinates (Figure 8). L_1 has a globally integrated circulation of 21 Sv and transports 0.10 Pg C_A yr^{-1} from the summer mixed layer depths (σ_0 = 25.0–26.7 kg m^{-3}) to the winter mixed layer depths (σ_0 = 26.7–27.8 kg m^{-3}, Figure 7 and Table 2). In the Southern Ocean this corresponds to a transport of C_A from TW into SAMW.

The L_2 cell reflects variability within the 10 year time period in the equatorial Pacific; and its transport is very small (less than 0.01 Pg C_A yr^{-1}) (Figure 6a). The L_3 cell is an anticlockwise cell occurring in the subtropics (Figures 4c, 5, and 6a). It mainly displays a density variability while the C_A content remains nearly constant, which reflects seasonal variations in freshwater fluxes. Precipitation leads to a decrease in density and dilution which reduces C_A concentrations, while evaporation has the opposite effect. L_3 has a globally integrated circulation of 7 Sv and transports 0.03 Pg C_A yr^{-1} due to the narrow spread of this cell in C_A space (Figure 7 and Table 2).

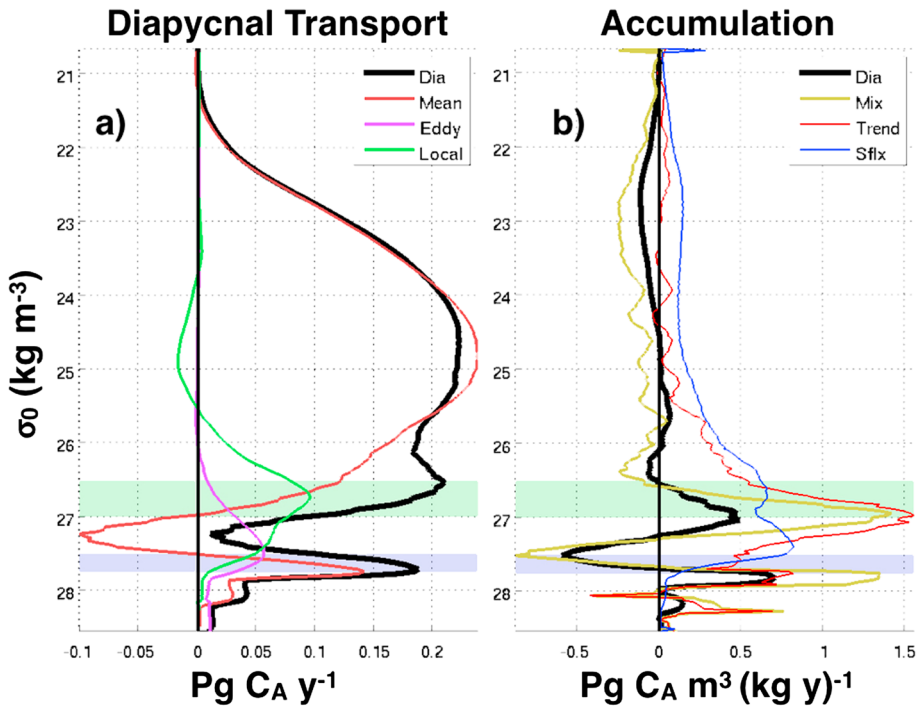

Figure 9. Diapycnal transport and accumulation rates, based on equations (9) and (10), respectively. (a) The diapycnal transport of C_A as a result of $\Psi^{mean}_{C_A\sigma_0}$, $\Psi^{eddy}_{C_A\sigma_0}$, $\Psi^{loc}_{C_A\sigma_0}$, and $\Psi^{dia}_{C_A\sigma_0}$. (b) The accumulation of C_A for each density class due to the $\Psi^{dia}_{C_A\sigma_0}$ (thick black line, which is the derivative of the black line of Figure 9a), air-sea C_A flux, diffusive mixing of C_A, and the trend. The air-sea flux (Sflx line) deposits C_A in the surface and the ocean circulation redistributes C_A (dia and mix lines) to give the density where C_A is accumulating (trend line). The color shading indicates water masses as in Figure 7c and Table 1. We used $\Delta\sigma_0 = 0.03$ kg m^{-3} and $\Delta C_A = 0.25$ mmol m^{-3}. The accumulation rates are smoothed with a running mean of 3 data points.

4. Diapycnal Transports and Accumulation

From the carbon-density stream functions we have calculated the diapycnal C_A transports (see equation (9)) for $e^{dia}_{C_A}$ (Figure 9a) and the accumulation rates for each component (Figure 9b).

The diapycnal transport $e^{dia}_{C_A}$ is always positive, leading to a net transport of C_A toward greater densities (black line; Figure 9a). However, individual contributions to diapycnal transport are not all positive. For the density range $\sigma_0 \approx 27-27.5$ kg m^{-3}, the Eulerian mean contribution (M_3 cell) results in large diapycnal transport toward lighter densities. This transport is opposed by local and eddy-induced transport (L_3 and E_1), such that the net diapycnal transport of C_A is always toward larger densities.

From the diapycnal transport, the accumulation of C_A due to redistribution in the ocean interior is calculated (Figure 9b). As the diapycnal transport is positive, diapycnal accumulation of C_A is due to a net inflow of C_A from lighter water, and reduction of C_A is due to a net outflow of C_A toward denser water. C_A accumulates mainly in two peaks between $\sigma_0 = 26.5-27.5$ kg m^{-3}, at the interface between SAMW and AAIW, and for $\sigma_0 > 27.75$ kg m^{-3}, related to NADW formation. The decomposition of the diapycnal accumulation shows that redistribution of C_A by eddies and cyclical motion of isopycnals are both first order processes for diapycnal C_A transports for $\sigma_0 > 26$ kg m^{-3} (Figure 7). This emphasizes the importance of having correct seasonal cycles and eddy advection scheme in a model.

The total accumulation of C_A is given by the sum of the diapycnal and trend accumulations which are driven by air-sea fluxes and diffusive accumulation terms (Figure 9b and Table 1). The peaks of accumulation of C_A due to the trend occur at the same density classes as diapycnal accumulation due to redistribution of C_A by ocean circulation. The ocean circulation generates accumulation pockets in the ocean interior, and the trend is accumulated in it. The trend peaks are, however, larger and range between $\sigma_0 = 26-28$ kg m^{-3}.

Air-sea fluxes mainly deposits C_A over a large density range, $\sigma_0 = 22-28$ kg m^{-3}. However, no increase in C_A is observed at the ocean surface for $\sigma_0 < 25$ kg m^{-3}, meaning that the C_A in this density range is redistributed

toward higher densities at the same rate as it is absorbed. This explains why the accumulation peak of the trend has a larger magnitude than that of the surface fluxes in the same density range (σ_0 =26.5 – 27.5 kg m^{-3}).

The mixing processes (calculated as a residual term) and ocean circulation explain the redistribution in density classes. Mixing processes concentrate the accumulation of C_A toward particular density ranges. C_A accumulation due to mixing shows two main peaks for σ_0 = 27 kg m^{-3} and σ_0 = 27.75 kg m^{-3}. The mixing processes are closely linked with the ocean circulation. Surface buoyancy fluxes and mixing lead to not only the M_1 cell that transports C_A from TW to mostly SAMW but also other subpolar mode waters. The C_A deposited at the surface of the Southern Ocean at σ_0 = 27.25 – 27.8 kg m^{-3} (dense AAIW/light CDW) is transformed into σ_0 =26.8 – 27.25 kg m^{-3} (light AAIW). For $\sigma_0 \approx$ 27.75 kg m^{-3}, the peak is due to processes at different geographical locations; the redistribution of C_A by NADW formation (M_2), eddies in the Southern Ocean (E_2), and mixed layer shoaling in the North Atlantic (L_1). These processes coincide with strong mixing to create a peak in the total accumulation for this σ_0 range (Figure 9b). The significant influence of NADW formation and potentially AABW on the C_A accumulation emphasizes the importance of deep water formation for C_A subduction.

The accumulation peaks for $\sigma_0 >$ 28 kg m^{-3} may be caused by the Veronis effect at depth (Figure 9b); i.e., the σ_0 surfaces are no longer aligned with the mixing direction, leading to spurious diapycnal transports. However, a component of this signal may be real and related to AABW formation.

5. Conclusion and Discussion

To analyze the surface to interior connections of C_A in the ocean, we developed and applied a new diagnostic tool that represents the ocean circulation in (C_A, σ_0) coordinates by means of a carbon-density stream function. The diagnostic tool is complementary to the Green Function methods in that it elucidates the pathways by which C_A is transported and accumulated in the ocean. While Green function methods provide an estimate of the time evolution of the net (or basin scale) ocean C_A inventory, they do not provide the means to understand the dynamics that control the water mass accumulation and redistribution of C_A in the ocean interior. The diagnostic method presented here analyzes the advection and tendency term on the LHS of equations (1) and (2), based on typically saved model fields, allowing us to decompose the C_A circulation into separate contributions from key processes such as the mean flow, eddy induced flow, seasonal cycle, and the trend in C_A concentration. *Iudicone et al.* [2011] typically analyzes the thermodynamic terms on the right-hand side of equations (1) and (2), both providing complimentary but different method to quantify the C_A circulation. The accumulation rates within certain density classes are calculated using these processes and are combined with the air-sea C_A fluxes to calculate C_A circulation by mixing processes and subsequently obtain a quantitative globally integrated C_A budget analyses. These analyses reveal pathways by which the C_A deposited at the surface of the ocean is transported into the ocean interior (Figure 10).

The net C_A uptake at the surface, over a wide σ_0 =21 – 28 kg m^{-3} range, is redistributed into the ocean interior by means of the circulation and mixing. As a result, the net increase of C_A in the ocean occurs in a much narrower σ_0 range associated with SAMW (28%) and AAIW (29%), with a peak at exactly their boundary at σ_0 =27 kg m^{-3}. Although there is also an uptake of C_A of 26% for σ_0<26.5 kg m^{-3}, this accumulation is predominantly due to the formation of SAMW from TW for σ_0 = 25.5 – 26.5 kg m^{-3}. Different mechanisms are suggested for the formation of SAMW. It is thought to be formed from either transformation of upwelled CDW at the surface [*Speer et al.*, 2000; *Sarmiento et al.*, 2004] combined with a contribution of returning subtropical gyre modified SAMW via the western boundary currents [*Sloyan and Rintoul*, 2001] or transformation of TW [*Iudicone et al.*, 2008b, 2011]. Our study suggests both mechanism are at play but with a dominant role for the transformation of SAMW from TW. The M_3 circulation does include some transformation, and related C_A transport, from CDW into SAMW (M_3 line in Figure 7a). The M_1 cell, however, has a larger C_A circulation associated with it and is predominantly due to the transformation of TW into SAMW (M_1 line in Figure 7a).

For the circulation in (C_A, σ_0) coordinates and related diapycnal C_A transports and redistribution, the Eulerian mean flow is the most dominant component. The main process for C_A circulation is that related to formation of SAMW from TW (M_1 cell) and formation of AAIW from CDW (M_3 cell). Our results agree with previous studies that find that mode waters are important for the ocean subduction of C_A [*Hanawa and Talley*, 2001; *Sallee et al.*, 2012; *Graven et al.*, 2012; *Levy et al.*, 2013].

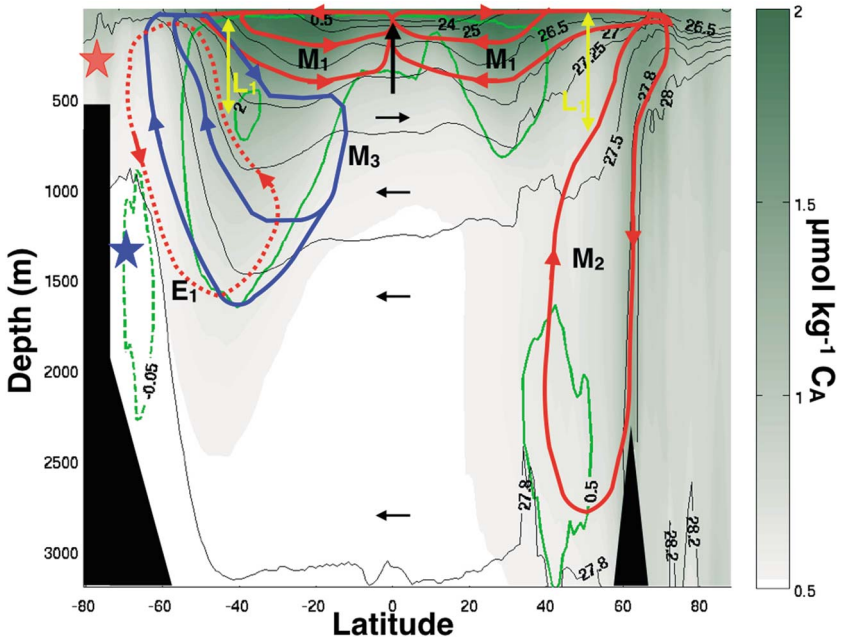

Figure 10. An overview of the processes identified in this model, using our diagnostic. The color of the ellipsis, indicated if the circulation is clockwise (red/yellow) or anti-clockwise (blue), like the colors in the stream function (Figures 3, 4). Cell E_1, L_2 and L_3 are not indicated as they are too small. The arrows on the ellipses indicate the direction of circulation. The black arrows represent the zonally averaged flow direction and the black contours are the zonally and time averaged surface referenced potential density anomaly (σ_0) contours. The solid (dashed) green contours are the positive (negative) zonally and time averaged C_A trend (Tg yr^{-1}). The shading (gray color bar) indicates the zonally and time averaged C_A concentration. The blue star and the red star indicate the location of the clockwise and anti-clockwise cycle, respectively, that is observed in these location in (Figure 6b) and discussed in the text.

The dominant role of the mean flow for the C_A redistribution, relates the ocean C_A uptake to the global meridional overturning circulation in the ocean [*Iudicone et al.*, 2011]. Since the large-scale ocean circulation is generally well captured by ocean models this explains why simulated oceanic C_A uptake is similar in these models [*Khatiwala et al.*, 2013], despite a poor representation of seasonality in many models [*Lenton et al.*, 2013]. However, it is clear from this study that both the eddy induced flow and the effects of seasonal cycles do have a significant contribution to C_A redistribution.

About 10% of the net increase in C_A is related to NADW and Antarctic bottom water (AABW) formation. In this study, these are the only ways to subduct C_A to depths greater than 1500 m and are therefore an important component of the C_A circulation and long-term sequestration.

The method used here could easily be applied to any model simulation to reveal C_A redistribution and provide a new way to assess and compare model simulations. Further, the method could be applied to future projections to show how the redistribution C_A changes with time. This method may also be applied to other tracers (e.g., dissolved oxygen and dissolved organic carbon) to better understand the circulations of these tracers. Finally, the diagnostic tool developed in this study has the potential to be applied to observations through the use of an inverse method, as done by *Groeskamp et al.* [2014b] for salinity and temperature coordinates or to the circulation field derived from tracer data [*Primeau et al.*, 2013]. This would provide an observational based assessment of the C_A circulation to compare to the results as shown here.

Acknowledgments
S.G. gratefully acknowledges support by the NASA grant NNX14AI46G and Lamont-Doherty Earth Observatory. S.G. was supported by the joint CSIRO Division-University of Tasmania Program in Quantitative Marine Science (QMS) and the CSIRO Division Wealth from Ocean flagship and through the OCE (Office of the Chief Executive) Science Team Postgraduate Scholarship Program and by the Centre of Excellence for Climate System Science. B.M.S., A.L., and R.M. was supported by the Australian Climate Change Science Program, jointly funded by the department of Climate Change and CSIRO Division. The model output that was used for this study can be obtained by sending a request (Andrew.Lenton@csiro.au). We thank Trevor McDougall for his involvement in initiating this project. We thank Daniele Iudicone for his comments that have significantly improved this manuscript.

References

Álvarez, M., et al. (2009), Estimating the storage of anthropogenic carbon in the subtropical Indian Ocean: A comparison of five different approaches, *Biogeosciences*, *6*(4), 681–703, doi:10.5194/bg-6-681-2009.

Boccaletti, G., R. Ferrari, A. Adcroft, D. Ferreira, and J. Marshall (2005), The vertical structure of ocean heat transport, *Geophys. Res. Lett.*, *32*, L10603, doi:10.1029/2005GL022474.

Bopp, L., M. Lévy, L. Resplandy, and J. B. Sallée (2015), Pathways of anthropogenic carbon subduction in the global ocean, *Geophys. Res. Lett.*, *42*(15), 6416–6423, doi:10.1002/2015GL065073.

Buckley, M. W., and J. Marshall (2016), Observations, inferences, and mechanisms of the Atlantic Meridional Overturning Circulation: A review, *Rev. Geophys.*, *54*(1), 5–63, doi:10.1002/2015RG000493.

Ciais, P., et al. (2013), Carbon and other biogeochemical cycles, in *Climate Change 2013: The Physical Science Basis. Contribution of Working Group I to the Fifth Assessment Report of the Intergovernmental Panel on Climate Change*, pp. 465–570, chap. 6, Cambridge Univ. Press, Cambridge, U. K., and New York.

Conkright, M. E., et al. (2002), *NOAA Atlas NESDIS 42*, 167 pp., NOAA, Silver Spring, Md.

Danabasoglu, G., et al. (2016), North Atlantic simulations in coordinated ocean-ice reference experiments Phase II (CORE-II). Part II: Inter-annual to decadal variability, *Ocean Modell.*, *97*, 65–90, doi:10.1016/j.ocemod.2015.11.007.

Döös, K., and D. J. Webb (1994), The deacon cell and the other meridional cells of the Southern Ocean, *J. Phys. Oceanogr.*, *24*(2), 429–442, doi:10.1175/1520-0485(1994)024<0429:TDCATO>2.0.CO;2.

Döös, K., J. Nilsson, J. Nycander, L. Brodeau, and M. Ballarotta (2012), The world ocean thermohaline circulation, *J. Phys. Oceanogr.*, *42*(9), 1445–1460, doi:10.1175/JPO-D-11-0163.1.

Downes, S. M., et al. (2015), An assessment of Southern Ocean water masses and sea ice during 1988–2007 in a suite of interannual CORE-II simulations, *Ocean Modell.*, *94*, 67–94, doi:10.1016/j.ocemod.2015.07.022.

Farneti, R., et al. (2015), An assessment of Antarctic circumpolar current and Southern Ocean meridional overturning circulation during 1958–2007 in a suite of interannual CORE-II simulations, *Ocean Modell.*, *93*, 84–120, doi:10.1016/j.ocemod.2015.07.009.

Ferrari, R., and D. Ferreira (2011), What processes drive the ocean heat transport?, *Ocean Modell.*, *38*(3–4), 171–186, doi:10.1016/j.ocemod.2011.02.013.

Gent, P. R., and J. C. McWilliams (1990), Isopycnal mixing in ocean circulation models, *J. Phys. Oceanogr.*, *20*(1), 150–155, doi:10.1175/1520-0485(1990)020<0150:IMIOCM>2.0.CO;2.

Gent, P. R., J. Willebrand, T. J. McDougall, and J. C. McWilliams (1995), Parameterizing eddy-induced tracer transports in ocean circulation models, *J. Phys. Oceanogr.*, *25*(4), 463–474, doi:10.1175/1520-0485(1995)025<0463:PEITTI>2.0.CO;2.

Graven, H. D., N. Gruber, R. Key, S. Khatiwala, and X. Giraud (2012), Changing controls on oceanic radiocarbon: New insights on shallow-to-deep ocean exchange and anthropogenic CO_2 uptake, *J. Geophys. Res.*, *117*, C10005, doi:10.1029/2012JC008074.

Groeskamp, S., J. D. Zika, T. J. McDougall, B. M. Sloyan, and F. Laliberté (2014a), The representation of ocean circulation and variability in thermodynamic coordinates, *J. Phys. Oceanogr.*, *44*(7), 1735–1750, doi:10.1175/JPO-D-13-0213.1.

Groeskamp, S., J. D. Zika, B. M. Sloyan, T. J. McDougall, and P. C. McIntosh (2014b), A thermohaline inverse method for estimating diathermohaline circulation and mixing, *J. Phys. Oceanogr.*, *44*(10), 2681–2697, doi:10.1175/JPO-D-14-0039.1.

Groeskamp, S., R. P. Abernathey, and A. Klocker (2016), Water mass transformation by cabbeling and thermobaricity, *Geophys. Res. Lett.*, *43*, doi:10.1002/2016GL070860.

Gruber, N., et al. (2009), Oceanic sources, sinks, and transport of atmospheric CO_2, *Global Biogeochem. Cycles*, *23*(1), GB1005, doi:10.1029/2008GB003349.

Hanawa, K., and L. D. Talley (2001), *Ocean Circulation and Climate*, chap. Mode Waters, 373–386 pp., Int. Geophys. Ser., Acad. Press.

Hieronymus, M., J. Nilsson, and J. Nycander (2014), Water mass transformation in salinity-temperature space, *J. Phys. Oceanogr.*, *44*, 2547–2568, doi:10.1175/JPO-D-13-0257.1.

Hirst, A. C., D. R. Jackett, and T. J. McDougall (1996), The meridional overturning cells of a world ocean model in neutral density coordinates, *J. Phys. Oceanogr.*, *26*(5), 775–791, doi:10.1175/1520-0485(1996)026<0775:TMOCOA>2.0.CO;2.

Iudicone, D., S. Speich, G. Madec, and B. Blanke (2008a), The global conveyor belt from a Southern Ocean perspective, *J. Phys. Oceanogr.*, *38*(7), 1401–1425, doi:10.1175/2007JPO3525.1.

Iudicone, D., G. Madec, and T. J. McDougall (2008b), Water-mass transformations in a neutral density framework and the key role of light penetration, *J. Phys. Oceanogr.*, *38*(7), 1357–1376, doi:10.1175/2007JPO3464.1.

Iudicone, D., K. B. Rodgers, I. Stendardo, O. Aumont, G. Madec, L. Bopp, O. Mangoni, and M. Ribera d'Alcala' (2011), Water masses as a unifying framework for understanding the Southern Ocean carbon cycle, *Biogeosciences*, *8*(5), 1031–1052, doi:10.5194/bg-8-1031-2011.

Kalnay, E., et al. (1996), The NCEP/NCAR 40-Year Reanalysis Project, *Bull. Am. Meteorol. Soc.*, *77*(3), 437–471, doi:10.1175/1520-0477(1996)077<0437:TNYRP>2.0.CO;2.

Key, R. M., A. Kozyr, C. L. Sabine, K. Lee, R. Wanninkhof, J. L. Bullister, R. A. Feely, F. J. Millero, C. Mordy, and T. H. Peng (2004), A global ocean carbon climatology: Results from global data analysis project (GLODAP), *Global Biogeochem. Cycles*, *18*(4), GB4031, doi:10.1029/2004GB002247.

Khatiwala, S., et al. (2013), Global ocean storage of anthropogenic carbon, *Biogeosciences*, *10*(4), 2169–2191, doi:10.5194/bg-10-2169-2013.

Kjellsson, J., K. Döös, F. B. Laliberté, and J. D. Zika (2013), The atmospheric general circulation in thermodynamical coordinates, *J. Atmos. Sci.*, *71*(3), 916–928, doi:10.1175/JAS-D-13-0173.1.

Laliberté, F., J. Zika, L. Mudryk, P. J. Kushner, J. Kjellsson, and K. Döös (2015), Constrained work output of the moist atmospheric heat engine in a warming climate, *Science*, *347*(6221), 540–543.

Le Quéré, C., et al. (2014), Global carbon budget 2014, *Earth Syst. Sci. Data Discuss.*, *7*(2), 521–610, doi:10.5194/essdd-7-521-2014.

Lenton, A., and R. J. Matear (2007), Role of the southern annular mode (SAM) in Southern Ocean CO_2 uptake, *Global Biogeochem. Cycles*, *21*, GB2016, doi:10.1029/2006GB002714.

Lenton, A., et al. (2013), Sea–air CO_2 fluxes in the Southern Ocean for the period 1990–2009, *Biogeosciences*, *10*(6), 4037–4054, doi:10.5194/bg-10-4037-2013.

Levy, M., L. Bopp, P. Karleskind, L. Resplandy, C. Ethe, and F. Pinsard (2013), Physical pathways for carbon transfers between the surface mixed layer and the ocean interior, *Global Biogeochem. Cycles*, *27*(4), 1001–1012, doi:10.1002/gbc.20092.

Marotzke, J., P. Welander, and J. Willebrand (1988), Instability and multiple steady states in a meridional-plane model of the thermohaline circulation, *Tellus A*, *40A*(2), 162–172, doi:10.1111/j.1600-0870.1988.tb00414.x.

Marshall, J., and K. Speer (2012), Closure of the meridional overturning circulation through Southern Ocean upwelling, *Nat. Geosci.*, *5*(3), 171–180.

Matear, R. J. (2001), Effects of numerical advection schemes and eddy parameterizations on ocean ventilation and oceanic anthropogenic CO_2 uptake, *Ocean Modell.*, *3*(3–4), 217–248, doi:10.1016/S1463-5003(01)00010-5.

Matear, R. J., and A. C. Hirst (1999), Climate Change Feedback on the Future Oceanic CO_2 uptake, *Tellus*, *51B*(3), 722–733.

Matear, R. J., and A. Lenton (2008), Impact of historical climate change on the Southern Ocean carbon cycle, *J. Clim.*, *21*, 5820–5834.

McDougall, T. J. (1987), Thermobaricity, cabbeling, and water-mass conversion, *J. Geophys. Res. Oceans*, *92*(C5), 5448–5464, doi:10.1029/JC092iC05p05448.

McNeil, B. I., and R. J. Matear (2013), The non-steady state oceanic CO_2 signal: Its importance, magnitude and a novel way to detect it, *Biogeosciences*, *10*(4), 2219–2228.

Mikaloff Fletcher, S. E., et al. (2006), Inverse estimates of anthropogenic CO_2 uptake, transport, and storage by the ocean, *Global Biogeochem. Cycles*, *20*(2), GB2002, doi:10.1029/2005GB002530.

Nurser, A. J. G., and M.-M. Lee (2004), Isopycnal averaging at constant height. Part I: The formulation and a case study, *J. Phys. Oceanogr.*, *34*(12), 2721–2739, doi:10.1175/JPO2649.1.
Nycander, J., J. Nilsson, K. Döös, and G. Broström (2007), Thermodynamic analysis of ocean circulation, *J. Phys. Oceanogr.*, *37*(8), 2038–2052, doi:10.1175/JPO3113.1.
Nycander, J., M. Hieronymus, and F. Roquet (2015), The nonlinear equation of state of sea water and the global water mass distribution, *Geophys. Res. Lett.*, *42*(18), 7714–7721, doi:10.1002/2015GL065525.
Pacanowski, R. C., and S. M. Griffies (1998), *Mom 3.0 Manual*, NOAA/GFDL, Princeton, N. J.
Primeau, F. W., M. Holzer, and T. DeVries (2013), Southern Ocean nutrient trapping and the efficiency of the biological pump, *J. Geophys. Res. Oceans*, *118*(5), 2547–2564, doi:10.1002/jgrc.20181.
Sabine, C., H. Ducklow, and M. Hood (2010), International carbon coordination: Roger Revelle's legacy in the intergovernmental oceanographic commission, *Oceanography*, *23*(3), 48–61.
Sabine, C. L., and other (2004), The oceanic sink for anthropogenic CO_2, *Science*, *305*(5682), 367–371.
Sabine, C. L., R. M. Key, A. Kozyr, R. A. Feely, R. Wanninkhof, F. J. Millero, T.-H. Peng, J. L. Bullister, and K. Lee (2005), Global ocean data analysis project (GLODAP): Results and data, Tech. Rep. ORNL/CDIAC-145, NDP-083, 110 pp., Oak Ridge National Laboratory, U.S. Department of Energy, Oak Ridge, Tenn.
Sallee, J.-B., R. J. Matear, S. R. Rintoul, and A. Lenton (2012), Localized subduction of anthropogenic carbon dioxide in the Southern Hemisphere oceans, *Nat. Geosci.*, *5*(8), 579–584.
Sarma, V. V. S. S., A. Lenton, R. M. Law, N. Metzl, P. K. Patra, S. Doney, I. D. Lima, E. Dlugokencky, M. Ramonet, and V. Valsala (2013), Sea–air CO_2 fluxes in the Indian Ocean between 1990 and 2009, *Biogeosciences*, *10*(11), 7035–7052, doi:10.5194/bg-10-7035-2013.
Sarmiento, J. L., N. Gruber, M. A. Brzezinski, and J. P. Dunne (2004), High-latitude controls of thermocline nutrients and low latitude biological productivity, *Nature*, *427*(6969), 56–60.
Schmidtko, S., G. C. Johnson, and J. M. Lyman (2013), Mimoc: A global monthly isopycnal upper-ocean climatology with mixed layers, *J. Geophys. Res. Oceans*, *118*(4), 1658–1672, doi:10.1002/jgrc.20122.
Schuster, U., et al. (2013), An assessment of the Atlantic and Arctic sea–air CO_2 fluxes, 1990–2009, *Biogeosciences*, *10*(1), 607–627, doi:10.5194/bg-10-607-2013.
Sloyan, B. M., and S. R. Rintoul (2001), Circulation, renewal and modification of Antarctic mode and intermediate water, *J. Phys. Oceanogr.*, *31*(4), 1005–1030.
Speer, K., S. R. Rintoul, and B. Sloyan (2000), The diabatic deacon cell, *J. Phys. Oceanogr.*, *30*(12), 3212–3222, doi:10.1175/1520-0485(2000)030<3212:TDDC>2.0.CO;2.
Stommel, H. (1948), The westward intensification of wind-driven ocean currents, *Eos Trans. AGU*, *29*(2), 202–206, doi:10.1029/TR029i002p00202.
Vage, K., R. S. Pickart, V. Thierry, G. Reverdin, C. M. Lee, B. Petrie, T. A. Agnew, A. Wong, and M. H. Ribergaard (2009), Surprising return of deep convection to the subpolar North Atlantic Ocean in winter 2007–2008, *Nat. Geosci.*, *2*(1), 67–72.
Veronis, G. (1975), *Numerical Models of Ocean Circulation*, chap. The role of models in tracer studies, 133–146 pp., National Academy of Science, Washington, D. C.
Wanninkhof, R., et al. (2013), Global ocean carbon uptake: Magnitude, variability and trends, *Biogeosciences*, *10*(3), 1983–2000.
Zika, J. D., M. H. England, and W. P. Sijp (2012), The ocean circulation in thermohaline coordinates, *J. Phys. Oceanogr.*, *42*(5), 708–724, doi:10.1175/JPO-D-11-0139.1.